Advanced Engineering Materials

ADVANCED ENGINEERING MATERIALS
www.aem-journal.com

RESEARCH ARTICLE OPEN ACCESS

Solid-State Diffusion and Intermetallic Phase Formation in Roll-Bonded Mg–Zn Composites With *Kirigami*-Patterned Inlay

Yaroslav Frolov[1] | Oleksandr Bobukh[2] | Christian Klose[1] | Florian Nürnberger[1] | Hans Jürgen Maier[1]

[1]Institut für Werkstoffkunde (Materials Science), Leibniz Universität Hannover, Garbsen, Germany | [2]Metal Forming Department, Ukrainian State University of Science and Technologies, Dnipro, Ukraine

Correspondence: Hans Jürgen Maier (maier@iw.uni-hannover.de)

Received: 10 November 2025 | **Revised:** 25 March 2026 | **Accepted:** 26 March 2026

Keywords: intermetallic phases | *kirigami* structure | Mg–Zn composites | roll bonding | solid-state diffusion

ABSTRACT

Solid-state diffusion and intermetallic phase formation were examined in roll-bonded magnesium alloy–zinc (Mg–Zn) composites that contain a *kirigami*-patterned magnesium alloy (ZX10) inlay. The *kirigami*-patterned inlay was embedded between two zinc sheets and roll-bonded at 310°C. Subsequent heat treatments at 318°C and 328°C promoted interfacial diffusion as well as the formation of intermetallic phases. The *kirigami* geometry of the inlay was employed as a process-level tool to impose spatially inhomogeneous deformation during roll bonding. This caused localized stress concentrations, driving the controlled transformation of the initial pattern within the deformation zone. It also prevented the thin inlay from failing prematurely and ensured its controlled distribution along the sample. Inhomogeneous strain distribution introduced three-dimensional diffusion pathways that activated bonding and initiated phase transformation. Flexural testing revealed a significant increase in mechanical strength compared to values calculated using the rule of mixtures. The maximum strength observed was 100 MPa for samples heat-treated at 318°C. Microstructural analyses showed a progression from adhesive bonding (group A) to uniform intermetallic layers (group B) and complex, multiphase regions containing eutectic, dendritic, and porous fractions (group C). Energy-dispersive X-ray spectroscopy confirmed zinc diffusion into the magnesium solid solution, indicating the onset of solid-state alloying. The combined effects of plastic deformation, thermal activation, and the *kirigami*-patterned Zn inlay resulted in Mg–Zn composites with enhanced interfacial integrity and a tailored phase composition. These composites offer a promising pathway for advanced material compounds to be used in biomedical and mechanical applications.

1 | Introduction

Both magnesium (Mg) and zinc (Zn) are widely researched in the context of biodegradable implant materials. The use of these elements as constituents of an alloy is attractive because they complement each other in terms of their corrosion behavior and mechanical properties, especially their ductility [1]. This can be achieved with up to 15 wt.% Zn in the binary system [2]. Increasing the Zn content in the alloy above 40 wt.% accelerates the growth of secondary phases and precipitation of Zn-rich particles, which could act as crack initiation sites [3]. Hu et al. [4] demonstrated that Zn content exerts a nonlinear effect on the mechanical properties of the Mg–Zn alloy: the flexural strength is 115 MPa at 10 at.% Zn, increases to 189 MPa at 20 at.% Zn, but decreases to 156 MPa at 30 at.% Zn. Such trends are inherent in alloys with Zn contents above 2.4 wt%, which are produced by metallurgical or sintering processes involving partial or total melting of the components [5]. Yet, increasing the Zn content continuously improves corrosion resistance. A way of improving the properties of Mg alloys with relatively low Zn

content is the addition of rare earth elements, which, due to their high valence, strong interatomic bonding, and slow diffusion rate in the Mg solid solution, provide advantages such as higher strength and greater thermal stability [6]. A case in point is Mg–Nd–Zn–Zr [7] alloys developed for bone screws. Table 1 summarizes the ranges of mechanical properties of Mg–Zn alloys and Mg–Zn-based composites reported earlier, together with brief notes on the key strengthening mechanisms and microstructural features.

Plastic deformation of Mg–Zn alloys as an alternative way to improve performance has been widely discussed in recent publications [7, 15]. Efficient plastic deformation techniques, such as equal channel angular extrusion [16] or accumulative roll bonding (ARB) [15] with subsequent heat treatment, appear to be promising for exploiting the synergy between Mg and Zn, especially in view of recent global restrictions on rare earth element trading. Rolling, in general, and ARB, in particular, are the most suitable techniques for obtaining flat Mg–Zn composite products [17]. Despite fine- grained size achieved and the homogeneous distribution of the microstructural constituents, these technologies have certain limitations. For instance, due to the kinematics of the deformation zone during rolling, low ductility of the final product results (<9% of residual elongation) [18], the challenge of obtaining thin sheets (<1 mm) persists [19], and the homogeneity of the layers' thicknesses [20] can be insufficient for a given application. The inhomogeneous stretching of layers with different ductility can explain these limitations [21]. Thermomechanical processes using continuous (solid) inlays and a high level of deformation to bond layers and modify the structure are unable to provide a stable distribution of the inlay along the length of the sample. This is because the thinning of the solid inlay stops after it fails during rolling. This effect has been shown for processes such as ARB, e.g., in [15]. On the other hand, regarding the roll bonding of different materials, strain inhomogeneity in the temperature range of hot deformation may initiate dynamic recrystallization in one of the layers, which could increase the diffusion rate. As shown by Mei et al. [22], roll bonding creates a high density of dislocations within a single material layer, facilitating faster diffusion at the interface to the adjacent material. Atoms or atomic clusters tend to accumulate near these dislocations, which provide for fast diffusion paths. From a kinetic point of view, the presence of dislocations and the increase in local temperatures due to severe plastic deformation may contribute to the faster diffusion of Mg atoms and promote the formation of Mg_xZn_y phases. Essentially, roll bonding of thin sheets generates additional dislocations at the interface due to strain inhomogeneity, which reduces the formation energy of intermetallic phases [23]. The inhomogeneous stretching of the inner layers that occurs during roll bonding can be explained by the dynamic instability of the speed balance, described as:

$$\frac{\delta_{\text{Core}}}{\delta_{\text{Shell}}} = \frac{v_{\text{Shell}}}{v_{\text{Core}}} \tag{1}$$

where δ_{Core} and δ_{Shell} are the residual elongation of both the core and the shell upon rolling and v_{Shell} and v_{Core} are the speeds of the respective layers along the rolling direction during roll bonding. Real rolling conditions of thin sheets are characterized by a large influence of friction on the stress–strain state in the deformation zone. Even a small deviation in surface and interface roughness, component thickness, or rolling gap can tip the balance of Equation (1) under these conditions. If $\frac{\delta_{\text{Core}}}{\delta_{\text{Shell}}} < \frac{v_{\text{Shell}}}{v_{\text{Core}}}$, excessive deformation will occur in the core; if $\frac{\delta_{\text{Core}}}{\delta_{\text{Shell}}} \gg \frac{v_{\text{Shell}}}{v_{\text{Core}}}$, necking up to failure is expected in the shell [24].

In the present study, Mg sheets of the intended solid-state alloyed composite were used as the *kirigami*-patterned inlay [25], in some sources called the kirigamized sheet [26]. The advantage

TABLE 1 | Mechanical property ranges of Mg–Zn alloys and composites reported in recent studies.

Alloy/Processing route	Key mechanical properties	Distinguishing features	Source
Zn–0.5 Mg, hot-rolled (50%–80% reduction)	UTS > 300 MPa; work hardening	Strengthening via grain refinement and Mg_2Zn_{11}/$MgZn_2$ intermetallics	[8]
Zn–0.6/1.3 Mg, hot-worked + hydrostatic extrusion	Compressive YS up to ≈350 MPa	Mg_2Zn_{11} particles pin grain boundaries, promoting strengthening	[9]
Mg–Zn binary alloys (powder metallurgy, biomedical)	Compressive stress ≈ 319 MPa; flexural strength ≈ 189 MPa; optimum at ≈ 20 wt.% Zn	Corrosion resistance improved with increasing Zn content up to ≈20 wt.%	[4]
Mg–Zn/Zn ARB composite	UTS ≈ 560 MPa; YS ≈ 540 MPa; $\varepsilon \approx 12\%$	In situ MgZn/Mg_2Zn nanoparticle formation; ultrafine grains (≈0.3 μm)	[10]
Mg–1Zn–0.2Ca–1MgO (extruded + aged)	YS ≈ 420 MPa; $\varepsilon \approx 12\%$	Ultrafine-grained structure (≈0.5–0.8 μm) with $Ca_2Mg_6Zn_3$ precipitates	[11]
Heterogeneous Mg–5.6Zn–0.6Zr	YS ≈ 345 MPa; UTS ≈ 370 MPa; $\varepsilon \approx 20.5\%$	Alternating coarse- and fine-grained "fibrous" layered microstructure	[12]
Mg–6Zn–Al–Ca + bimodal SiC	YS ≈ 322 MPa; UTS ≈ 360 MPa	Grain size refined to ≈0.9 μm; combined particle and precipitate strengthening	[13]
Mg–4Zn–0.6MgO	UTS ≈ 150 MPa	Nanoparticle load transfer; improved corrosion resistance	[14]

of the *kirigami*-patterned inlay arises because the cuts partition the sheet into regions with differing stress sensitivity, i.e. high-stress and low-stress zones [27]. The pattern also provides additional stress-relief mechanisms: line bending (i.e., opening of cuts along the rolling direction) and stretching in directions not parallel to the rolling direction, which reduces the component v_{Core} in Equation (1). This prevents the less ductile Mg inlay from failing prematurely and ensures its controlled distribution along the sample length. The positive effect of this approach is reflected in improved bond quality and a significant enhancement of the mechanical performance of Al–Mg composites [28]. This also provides a scalable and straightforward approach to impart deformability beyond that of the base material, which is important for Mg, given its low ductility.

It was expected that roll bonding of Mg–Zn composites would provide a promising pathway to form intermetallic phases at the interface through strain-induced diffusion by a high level of deformation without failure, characterized by multiple flow directions and increased dislocation densities and lattice mismatches. Together with local strain-induced overheating, this accelerates intermetallic phase formation, even without additional heat treatment, by reducing the formation energy [23].

Applying *kirigami* patterning to the Mg layer prior to roll bonding with Zn sheets, as a novel process-level tool to control deformation and activate three-dimensional diffusion pathways, should enhance interfacial bond quality by promoting strain-induced diffusion during roll bonding, thereby facilitating the formation of graded Mg–Zn intermetallic phases. It was further hypothesized that post-deformation heat treatment would amplify the formation of intermetallics without compromising the structural integrity of the thin composite sheet, which aligns with the overall objective to create composites that combine the higher strength of Mg with the slower degradation rate of Zn.

Against this background, this study investigates how a *kirigami*-patterned Mg sheet inlay, whose geometry induces a controlled, complex stress–strain state in the deformation zone, together with targeted heat treatment, influences intermetallic phase formation and the mechanical properties of roll-bonded Mg–Zn composites, with the aim of increasing composite strength and promoting controlled solid-state alloying via localized activation of interfacial diffusion.

2 | Experimental Section

2.1 | Roll-Bonding of Conventional Zn–ZX10–Zn Composites

The chemical composition of the sheet materials is given in Table 2. First, a three-layer Zn–ZX10–Zn assembly was roll-bonded. This consisted of two outer 0.25 mm thick layers of Zn and one internal layer of a ZX10 alloy with a thickness of 0.15 mm. This composite served as a reference that did not use the *kirigami* approach.

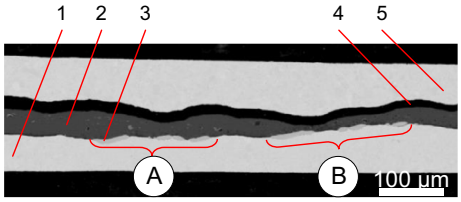

FIGURE 1 | Longitudinal section of a partly delaminated roll-bonded Zn–ZX10–Zn composite: A and B mark zones where intermetallic phases were observed; 1 – lower Zn shell; 2 – Mg alloy core; 3 – intermetallic phase; 4 – delamination gap; 5 – upper Zn shell.

This three-layer assembly was roll-bonded at 300°C using 200 mm diameter rolls, with a reduction of approximately 65%. Figure 1 shows a cross-section of the resulting Zn–ZX10–Zn composite. In this case, partial delamination of the nonpatterned Mg alloy sheet after roll bonding is obvious. This demonstrates that the balance expressed in Equation (1) was not met. Moreover, Figure 1 exhibits clearly visible areas that contain intermetallic phases at the interface, even without additional heat treatment. These areas marked A and B in Figure 1 correspond to excessive deformation of the Mg alloy inlay caused by the above-mentioned imbalance. In zone A, the Mg alloy layer is thinned by approximately 40% compared to the average thickness of the inlay; in zone B, the thinning reaches 65%. Defects at the edges of the Mg alloy inlay further confirm the significant strain heterogeneity during roll bonding (Zone B in Figure 1).

2.2 | Roll-Bonding of Zn–ZX10–Zn Composites With *Kirigami*-Patterned Inlay

A schematic illustrating the roll bonding of the composites with the *kirigami*-patterned inlay is shown in Figure 2. For these experiments, the initial materials had the same chemical composition as used for the reference, cf. Table 2. However, these strips were produced using a combination of hot and cold rolling, followed by annealing. Thus, the ZX10 strip had a thickness of 0.15 mm, but the pure Zn strips were 0.27 mm thick.

The ZX10 alloy strips were punched with 4 mm diameter holes, spaced 3 mm apart. The rows with holes were aligned such that no spacing was provided between the rows of holes, cf. Figure 2c. This arrangement ensured a uniform transparency of approximately 50% (material-to-hole area ratio). The *kirigami* inlay geometry was chosen based on (i) practical experience with roll bonding of *kirigami* inlays across different materials [29, 30], (ii) the formulation of a uniform-deformation criterion for the *kirigami* structure within the rolling deformation zone [28], and (iii) the need to avoid stress concentrators associated with

TABLE 2 | Chemical composition of sheet materials in wt.% measured using a SPECTROMAXx LMX06 spark optical emission spectrometer.

	Zn	Mg	Al	Fe	Cu	Si	Ca
Zn	balance	0.004	0.003	0.0025	0.0005	0.0007	—
ZX10	1.07	balance	0.03	0.045	0.02	0.02	0.36

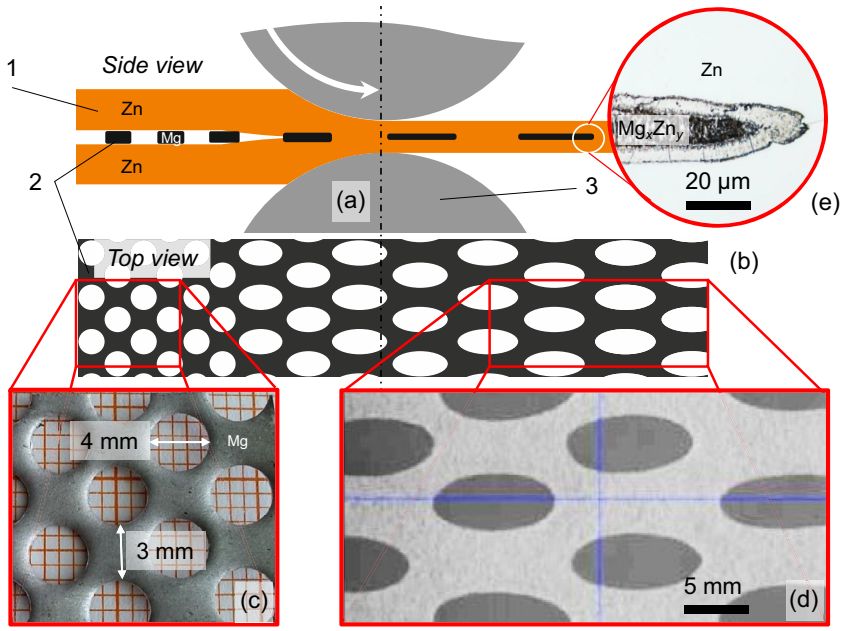

FIGURE 2 | (a) Schematic of the roll bonding of Zn sheets (1) with *kirigami*-patterned Mg-alloy inlay (2) with two rolls (3); (b) longitudinal section of the deformation zone with pattern changing during deformation; (c) top view of *kirigami*-patterned Mg alloy inlay; (d) X-ray image of the roll-bonded composite; (e) light microscopic image of the inlay inside the Zn layer after roll bonding and heat treatment.

traditional *kirigami* cuts, which are particularly detrimental in thin films.

The geometric changes to the shape of the deformed Mg alloy inlay were analyzed using X-ray imaging (see Figure 2d), while the longitudinal cross-section of the composite was examined using optical microscopy (see Figure 2e).

Prior to rolling, the surface of the samples was degreased and then ground with 400-grit sandpaper. Rolling was carried out at 310°C on a two-roll mill with a roll diameter of 200 mm at a speed of 0.29 m/s according to the following sequence:

$$\mathrm{Zn}_{0.27} + \mathrm{ZX10}_{0.15} + \mathrm{Zn}_{0.27} \rightarrow \mathrm{Zn}_{0.12} + \mathrm{ZX10}_{0.08} + \mathrm{Zn}_{0.12} \rightarrow \mathrm{Zn}_{0.08} + \mathrm{ZX10}_{0.05} + \mathrm{Zn}_{0.08}$$

where the indices following the material designation refer to the thickness of the corresponding layer in mm.

The composites' total thickness after the first pass was 0.32 mm, and the bonds were stable. Yet, it was still easy to separate such a composite by hand. Composites with a thickness of 0.21 mm, characterized by a strong bond, were obtained after the second rolling pass. Attempts to delaminate such a composite resulted in its fracture. Following the rolling process, all the composites were then subjected to a thermal treatment at a temperature of 310°C for a duration of 10 min. At this point, the composites were categorized into three distinct groups:

- Group A: no further treatment after roll bonding and annealing
- Group B: heat-treated for 30 min. at 318°C
- Group C: heat-treated for 20 min. at 328°C.

This temperature range corresponds to a critical region of the Mg–Zn phase diagram at around 325°C, where diffusion is strongly activated, and the stoichiometry of the intermetallics can change. This makes their formation sensitive to local chemical composition and deformation-induced defects. Accordingly, a rolling temperature of 310°C was chosen to avoid these effects and enable pure mechanical bonding. The temperature of 318°C exhibits a low-temperature region where the stoichiometry of the intermetallic phases should remain mostly unaffected. In contrast, the temperature of 328°C corresponds to a high-temperature area that is limited by the eutectic point at 340°C. A solid-state change in the intermetallic stoichiometry is expected here.

The average density of the composites was $6.1 \pm 0.1\ \mathrm{g/mm^3}$, corresponding to 86 ± 2% of the density of pure Zn irrespective of the heat treatment parameters. The variation within each group was similar to the variation between groups A, B, and C.

The volumetric fraction of the inlay structure in the composite can be calculated using a mass balance:

$$m_C = m_M + m_{In} \tag{2}$$

where m_M is the mass of the two Zn matrix layers, m_{In} is the mass of the embedded ZX10 *kirigami* inlay, and m_C is the total mass of the composite. Equation (2) can be expressed in terms of volume and density as:

$$m_C = V_C \times \rho_C = (V_M \times \rho_M) + (V_{In} \times \rho_{In}) \tag{3}$$

where V_M and V_{In} are the volumes of the Zn matrix and the ZX10 *kirigami* inlay, respectively, and ρ represents the corresponding densities. Assuming the total volume of the composite V_C is 100%, Equation (3) can be rearranged to determine the volumetric fraction of the ZX10 inlay:

$$V_{In(\%)} = \frac{\rho_M - \rho_C}{\rho_M - \rho_{In}} \times 100\% \tag{4}$$

Given the measured composite density of $\rho_C = 6.1\,g/mm^3$, and the densities of Zn and ZX10 being equal to $\rho_M = 7.1\,g/mm^3$ and $1.8\,g/mm^3$, respectively, the calculated volumetric fraction of the ZX10 phase in the composite is $18\% \pm 2\%$.

The experimental procedure resulted in the following specimens, which were subsequently subjected to mechanical testing: pure Zn after rolling and annealing; group A composite after rolling; group B composite after roll-bonding and annealing at 318°C; group C composite after rolling and annealing at 328°C; and ZX10 after rolling and annealing. Furthermore, the measured volumetric fractions of the constituent phases allowed a virtual composite to be constructed, the mechanical properties of which were predicted using the rule of mixtures.

2.3 | Three-Point Bending Tests

For consistent comparability among thin composites with varied cross-sectional structures, flexural (bending) testing was chosen to circumvent the susceptibility of thin-specimen tensile tests to cross-sectional definition, size effects [31], and grip-related artifacts [32]. Three-point bending tests were used to investigate the mechanical properties of the obtained composites (groups A, B, and C), as well as their constituent components (Zn and the ZX10 alloy). For these tests, a Zwick/Roell Retroline Z010 universal testing machine was used with a load cell sensitivity threshold of 0.2 N, a span between supports of 20 mm, and a loading edge with a diameter of 5 mm. The preloading was set at 0.5 N, and the loading edge moved at a speed of 1 mm/s. Flexural stress was calculated according to the standard ISO 178:

$$\sigma_f = \frac{3FL}{2bh_i^2} \tag{5}$$

where F is the applied force in N; L is the span length between supports in mm; b is the specimen width in mm, and h_i is the specimen thickness in mm. Since the ISO 178 protocol does not require specimen to fracture, maximum flexural stress was primarily used as a comparative metric to evaluate the impact of heat treatment and interfacial microstructure on Zn–Mg–Zn composites.

2.4 | Microstructural Analysis of the Composites

The microstructure of the ZX10 inlay within the Zn layer of groups A, B, and C composites was characterized using a ZEISS Supra 55 VP field emission scanning electron microscope (SEM) in low-vacuum mode, equipped with a backscattered electron detector (BSD). The imaging conditions were set to an accelerating voltage of 15 kV, a probe current of 1.7 nA, and a working distance of 8.8 mm. The BSD provided compositional contrast between the Zn layer and the Mg-containing phases. This made it possible to highlight intermetallics and microstructural features across the composite cross-sections. Energy-dispersive spectroscopy (EDS) was used to probe chemical composition with high lateral resolution. It should be noted that EDS does not allow to directly distinguish between different phases of similar composition. Instead, it only indicates if a certain analysis stoichiometrically corresponds to a given phase, according to the Mg–Zn phase diagram. Thus, the present approach cautiously interprets interfacial evolution and assesses the likelihood of certain phases forming under the relevant thermodynamic conditions.

3 | Results

3.1 | Three-Point Bending Test

The dimensions of the samples were $40\,mm \times 15\,mm \times 0.15$–$0.21\,mm$. Thickness variations resulted from the rolling of different materials. However, the deviation in thickness across the length and width of each sample did not exceed 0.01 mm. The actual sample thicknesses used for testing were as follows: Group A, B, and C composites - 0.21 mm; Zn - 0.2 mm; ZX10-0.15 mm. It should be noted that even small differences in thickness influence the strain calculations. Thus, the changes in flexural stress along the movement of the loading edge (shown in Figure 3) are presented relative to a punch displacement of 10 mm. For comparison, the rule of mixtures was used to estimate the strength $\sigma_{fcalc.}$ of the composites containing 82% Zn and 18% of the ZX10 alloy:

$$\sigma_{fcalc.} = \sigma_{fZn} \times 0.82 + \sigma_{fZX10} \times 0.18 \tag{6}$$

where σ_{fZn} and σ_{fZX10} are the values of flexural stress of the corresponding single materials (Zn, ZX10) at the same loading edge position. This corresponds to a reference material state without intermetallic phase formation. It should be noted that the rule of mixtures does not account for interfacial reaction products or local defects. Instead, differences between the theoretical strength calculated this way and the measured values point to effects arising from the *kirigami* inlay geometry, three-dimensional interfacial interactions, and deformation-induced microstructural evolution.

As expected, the flexural strength curves showed that the ZX10 alloy had the largest area under the curve, indicating the greatest

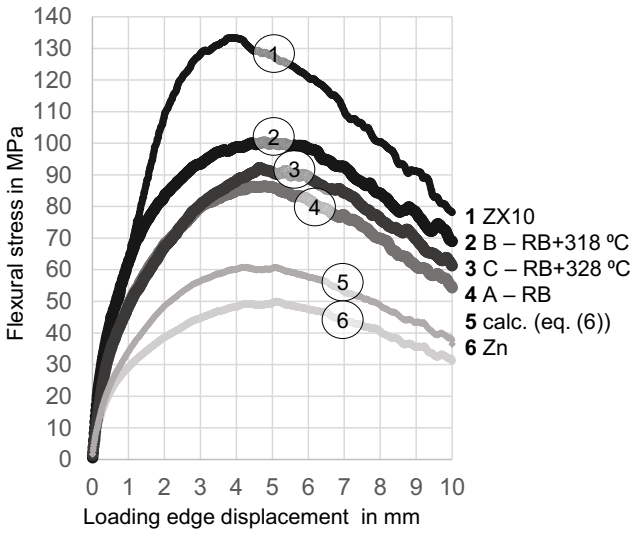

FIGURE 3 | Flexural stress–displacement curves for roll-bonded Mg–Zn composites with *kirigami*-patterned inlays, along with their constituent components, averaged across each test series: 1 – ZX10; 2 – group B; 3 – group C; 4 – group A; 5 – calculated value for a combination of 82% Zn and 18% ZX10; 6 – pure Zn.

deformation work, whereas the Zn sample displayed the smallest area. The composites were positioned between these two boundaries, cf. Figure 3. Notably, none of the samples exhibited a sudden drop in load during testing, which demonstrates the stability of the samples. This is particularly significant given that samples within groups A, B, and C were arranged so that the loading edge engaged different elements of the *kirigami*-patterned inlay.

Table 3 presents the maximum flexural stress values and the corresponding loading edge displacements. Each test series included three specimens. The standard deviation of these data remained below 9.5%. The *t*-test at 0.05 showed that the differences in maximum stress among groups A, B, and C are statistically significant, confirming substantial differences in their mechanical properties.

3.2 | Microstructural Analysis

SEM images of the ZX10 inlay in a Zn matrix for composites of groups A, B, and C are shown in Figure 4. For group A, i.e. roll bonding and annealing already resulted in a joint with some structural integrity, but metallurgical bonding had not been established yet (Figure 4a). The intermetallic layer was either missing or extremely thin, and the interface between Mg and Zn was sharp and well-defined, without detectable interdiffusion.

Additional thermal treatment at 318°C for 30 min (group B) promoted interfacial diffusion, resulting in the formation of an approximately 12–18 µm thick intermetallic layer. This layer predominantly formed on the Zn side of the interface, increasing the total thickness of the *kirigami* structure to approximately 70 µm (Figure 4b). The intermetallic layer exhibited a relatively uniform morphology, with slight waviness at the phase boundaries, which is characteristic of diffusion-controlled growth.

The heat treatment involving exposure at 328°C for 20 min (group C) resulted in the formation of a complex, multiphase structure within the Mg alloy inlay and adjacent intermetallic layers. This structure had a total thickness of ≈80 µm (Figure 4c). EDS elemental mapping of the interfacial reaction zone (Figure 4d) shows extensive Zn enrichment within regions previously occupied by the Mg alloy. The Zn distribution is heterogeneous, with composition gradients and transition regions of lower Zn content. Layers adjacent to the Zn shell and the Mg inlay exhibit compositions consistent with thermodynamically stable Mg–Zn intermetallic phases. The central region displays a porous, dendritic/needle-like to columnar morphology, consistent with formation under local thermal excursions followed by rapid cooling. This region is expected to represent either a eutectic mixture or a porous phase structure formed by nonuniform diffusion or a reactive diffusion front. The presence of vertical channels or voids within the structure may indicate incomplete phase coalescence or localized stress development during rapid cooling. Thus, relatively thick (≈40% of the total strip thickness) and morphologically complex intermetallic layers form within the composite at higher temperatures, indicating intense interfacial interaction characteristic of fully developed solid-state diffusion with the complete dissolution of the metallic Mg alloy inlay.

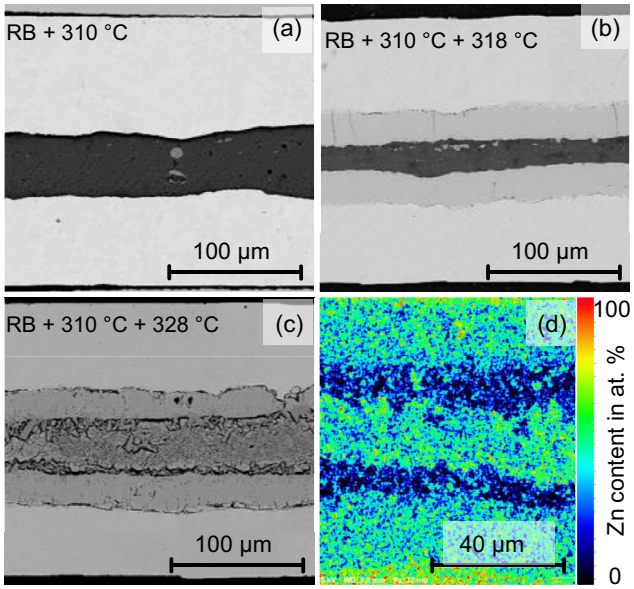

FIGURE 4 | SEM micrographs showing the ZX10 inlay embedded within the Zn matrix after roll bonding and subsequent heat treatments: (a) group A – roll bonding followed by annealing; (b) group B – same as group A, but with additional heat treatment at 318°C for 30 min; (c) group C – same as group A, but with additional heat treatment at 328°C for 20 min; (d) EDS mapping of the inlay area of the specimen of group C.

The effect of heat treatment of group B and C composites on the mutual diffusion of Mg and Zn was quantified using an EDS analysis of the intermetallic zone. Figure 5 shows the results of the EDS line scan analysis along the cross-section of the diffusion zone between the Zn matrix and the ZX10 alloy *kirigami* inlay, for samples from groups B and C. After heat treatment at 318°C for 30 min, the group B sample develops a distinct 17 µm intermetallic layer with $MgZn_2$ stoichiometry; toward the Zn

TABLE 3 | Flexural performance of composites and their components.

Material, group, or calculated value	Position in Figure 3	$\sigma_{f\,max}$ in MPa	Loading edge displacement to $\sigma_{f\,max}$ in mm
ZX10	1	133.2 (± 6.3)	3.83 (± 0.18)
Group B	2	100.3 (± 5.2)	4.77 (± 0.25)
Group C	3	92.2 (± 6.5)	4.67 (± 0.33)
Group A	4	86.4 (± 4.5)	4.26 (± 0.22)
$\sigma_{fcalc.}$ (Equation (6))	5	64.7	4.19
Zn	6	49.9 (± 1.9)	5.11 (± 0.20)

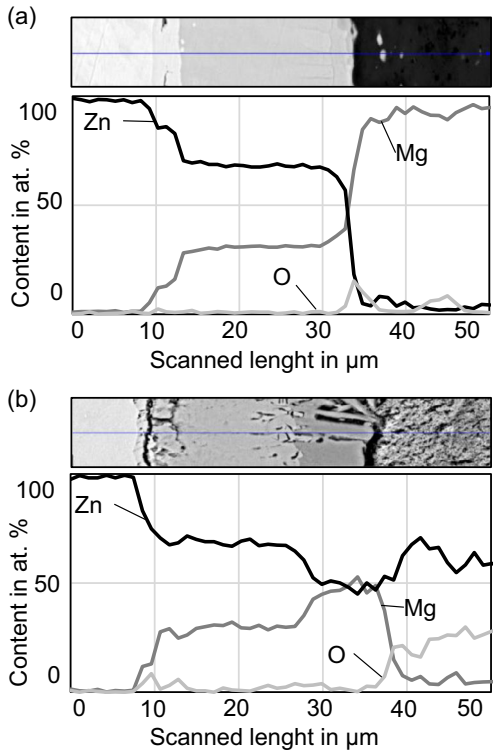

FIGURE 5 | Results of EDS line scan analysis of the diffusion zone for samples from group B, roll-bonded with subsequent heat treatment at 318°C for 30 min (a), and group C, roll-bonded with subsequent heat treatment at 328°C for 20 min (b). The SEM images of the corresponding scan areas are shown above the scans, along with the line along which the analysis was performed.

side, this is replaced by a 2–3 µm transition zone corresponding to Mg_2Zn_{11}. On the Mg side, the phase, stoichiometrically corresponding to Mg_2Zn_3, is present, along with a sharp transition to metallic Mg. The position of the interface from which diffusion began is indicated by the increase in oxygen concentration at 33 µm of the line scan length (Figure 5a).

The samples from group C, which were heat-treated at 328°C for 20 min, revealed a much more complex picture. In the region up to 35 µm in Figure 5b, there is an increase in Mg concentration: up to 8 µm, there is a weak increase apparently within the limits of a Mg–Zn solid solution. From 8 to 11 µm, there is a transition zone that stoichiometrically corresponds to the Mg_2Zn_{11} phase. Between 11 and 26 µm, lies a stable intermetallic zone, which stoichiometrically corresponds to $MgZn_2$, and from 27 to 35 µm, a transition zone with an increased Mg concentration is observed that can be described as a mixture of Mg_2Zn_3 and MgZn. In the area beyond 35 µm, the Zn content increases significantly while the magnesium concentration decreases accordingly. This unexpected effect may be due to Zn diffusion into the inlay caused by magnesium deficiency resulting from the intense formation of intermetallic phases in the Zn matrix. The sharp increase in oxygen content at the 38 µm mark suggests that this was initially the interface between the magnesium *kirigami* inlay and the Zn matrix. In parallel, an increased oxygen content to ≈25 at.% was recorded in the 38–50 µm zone. This is probably due to the secondary oxidation of magnesium, the formation of residual oxides, or the diffusion of oxygen along grain boundaries. Consequently, the zone beyond 35 µm of the scanned length in group C exhibits an expanded multiphase structure comprising intermetallic phases, eutectic phases, and composition gradients, all of which are distinctive features of an active solid-state diffusion joint involving high-temperature Mg–Zn interaction. The experimental results reveal a direct correlation between heat-treatment parameters, interfacial microstructure, and flexural performance. Moderate annealing at 318°C for 30 min (Group B) results in the formation of a relatively uniform intermetallic layer with a thickness of 12–18 µm and yields the highest flexural strength among the composites (100 MPa), exceeding both Group A (86 MPa) and the composite strength of 65 MPa calculated from Equation (6) . Increasing the thermal exposure to 328°C for 20 min (Group C) promotes the development of a much thicker (≈80 µm) and morphologically complex multiphase intermetallic zone, accompanied by extended diffusion lengths and partial depletion of the Mg inlay. The presence of this zone can be visually detected as a dark *kirigami* pattern on the specimen's surface (Figure 6a).

Despite intensified solid-state diffusion, this structural overdevelopment coincides with a reduction in flexural strength to 92 MPa, indicating a trade-off between intermetallic layer thickness and mechanical stability. Faster Zn diffusion into Mg than vice versa results in a vacancy-flux imbalance and Kirkendall porosity on the Mg side, consistent with Zn enrichment in regions formerly occupied by Mg and elevated oxygen/porosity at these positions (25%–27%). The interfacial phase sequence corresponds to the Mg–Zn phase diagram (Zn-rich intermetallics near Zn, progressively Mg-richer toward Mg), and the thickness increase from ≈17–18 µm at 318°C to ≈80 µm at 328°C is in accordance with diffusion-controlled, defect-assisted growth under rolling conditions. The porous, dendritic/columnar morphologies in Group C are consistent with local thermal fluctuations near the eutectic and a complex multiphase reaction zone. Together, these mechanisms explain the reduced flexural strength in Group C via a thick, brittle intermetallic layer and Kirkendall porosity that reduce the effective load-bearing cross-section and promote strain localization and interfacial cracking. Figure 6b shows the development of strain-induced cracks within this layer. Because the Kirkendall voids lie adjacent to the Zn layer, they appear to hinder crack transmission into the Zn layer, redirecting deformation along the three-dimensional porous interface. Consequently, the fracture tends to localize within the *kirigami* inlay due to its low ductility, while the Kirkendall–porous interface effectively decouples from the Zn shell.

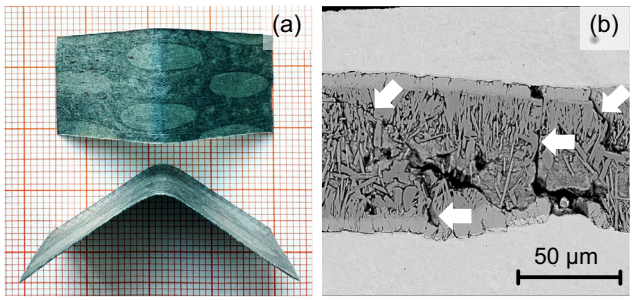

FIGURE 6 | Samples of Group C: (a) unfractured specimens after the three-point bending test; (b) after 10% cold reduction; arrows indicate cracks in the former Mg layer.

4 | Discussion

All composites demonstrated flexural strength that exceeded the theoretically calculated value by 34%–55%, a result of the *kirigami* structure of the Mg alloy inlay and the heat treatment for groups B and C. The composite of group B showed the highest flexural strength (100 MPa, or 155% of the theoretical value), due to the formation of a homogeneous intermetallic layer with a clear phase sequence of Mg_2Zn_{11}-$MgZn_2$-Mg_2Zn_3 as a result of the heat treatment at 318°C.

As pointed out, the phases were inferred based on the Mg–Zn phase diagram and on stoichiometry as determined by EDX analysis. Work is underway to confirm phase constitution, particularly in the multiphase region of Group C, by X-ray diffraction and transmission electron microscopy.

The Mg alloy layer's *kirigami* structure led to predominantly adhesive bonding in group A. This resulted in a 34% increase in the theoretical flexural strength up to 82 MPa.

Advanced flexural-stress models that account for intermetallic layers, interfacial bonding, and porosity would likely improve predictive accuracy; their development could be advanced as part of future work on Mg–Zn layered *kirigami* composites, in which failure modes and interfacial cracking are investigated for various intermetallic morphologies using SEM.

Compared with Group B, the reduced flexural properties in Group C can be attributed to a diminished effective load-bearing cross-section caused by enhanced porosity and oxidation in the former Mg region (Figure 5b), where the oxygen content reaches 25%–27%, and by Kirkendall voiding. The mechanistic roles differ: intermetallic brittleness and oxidation nucleate cracks within the *kirigami* inlay, whereas Kirkendall porosity promotes their deflection and evolution into interfacial delamination (Figure 6b). Group C shows a morphologically complex multiphase structure with eutectic phases [33], porosity, and deep diffusion of Zn into the Mg inlay. An increase in the diffusion coefficient of Zn in Mg after ARB over a comparable temperature range has been reported in [34]. EDS analysis results confirmed that the intermetallic zone in group C completely covers the Mg alloy inlay and includes substitutional diffusion of Zn into Mg. Due to the higher heat treatment temperature (328°C) and the specific *kirigami* architecture, an extended multiphase transition zone formed in group C, showing signs of solid-state alloying as well as changes in the microstructure, mechanical properties, and phase composition of the material. Similar evidence of solid-state alloying in an Al–Mg alloy processed by ARB has been reported in [22]. The *kirigami* geometry of the Mg inlay (Figure 7), embedded within the Zn matrix during roll bonding and subsequent heat treatment, enables mutual diffusion in three dimensions, in contrast to conventional planar interfacial diffusion. The intermetallic layer grown along the rolling direction is approximately twice as thick as that observed in the transverse cross-section, highlighting the dominant role of strain-induced effects in intermetallic growth in addition to purely thermal contributions. This also indicates that overcoming reaction limitations at the interfaces is not a key contribution in this case.

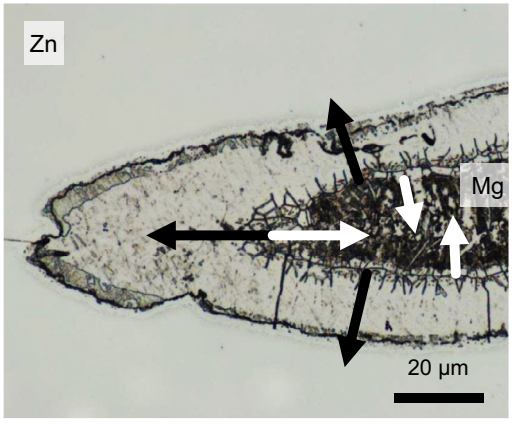

FIGURE 7 | Optical image illustrating mutual diffusion of Mg (black arrows) and Zn (white arrows) in the composites with a *kirigami*-patterned inlay made of ZX10 alloy.

The sensitivity of the deformed structure to temperature [35] and uneven heat transfer in the body of the *kirigami* structure leads to the activation of both surface and internal substitutional diffusion. This results in the appearance of eutectic, columnar intermetallic phases as well as porosity in the central zone of the inlay, cf. Figure 4c. EDS analysis confirmed that Zn had diffused to the full depth of the Mg layer, which indicates that the initial inlay had been completely restructured. Such substitutional diffusion of Zn into the Mg crystal lattice is associated with the Kirkendall effect and is theoretically described by Yu et al. [36] The simulation results presented by Chen et al. [37] show that elements such as Mn, Cu, and Ag significantly reduce Mg vacancy diffusion in Zn. Despite a lack of available data on the vacancy diffusion in the reciprocal (Zn → Mg) direction, this may explain the uneven growth of intermetallic phases in the Mg–Zn system. Thus, the metallurgical prerequisites for diffusion development can be met by using a 3D interface configuration and by saturating the near-surface layers with crystal lattice defects. Both of these factors are determined by the thermal-deformation regime of roll bonding. Such complex interactions; however, require further study, particularly with regard to the temperature and strain parameters of roll bonding. These are key factors that impact the intensity and direction of diffusion, and consequently the final phase composition of the composite.

The results of the present study are specific to the Mg–Zn system and the investigated *kirigami* geometry; therefore, the quantitative values of intermetallic thickness, phase distribution, and mechanical response can not be directly generalized. The identified mechanism, i.e. activation of solid-state diffusion through spatially inhomogeneous deformation, defect enrichment, and three-dimensional interface topology, represents a process-level concept supported with a material-specific effect. Thus, the applicability of this approach to other material systems is expected to depend on their mutual diffusion behavior, intermetallic-forming tendency, and deformation compatibility. Work is underway to address this in other systems.

5 | Conclusions

1. *Kirigami*-assisted roll bonding is a process-level tool promoting solid-state diffusion and controlled intermetallic formation at Mg–Zn interfaces within a

limited thermomechanical window. This enabled three-dimensional diffusion and intermetallic layers ranging from below the detection limit to ≈ 80 μm. This correlates with an initial increase and subsequent decrease in flexural strength. While deformation-induced solid-state alloying is feasible, intermetallic control remains highly dependent on processing conditions and geometry.

2. A *kirigami*-patterned inlay relieves local stresses and prevents fracture when bonding a Mg core to a Zn shell, ensuring stable contact and increasing bending strength by ≈73% versus pure Zn. It reduces density to 6.1 ± 0.1 g/cm^3 (≈14% lower than Zn). Even without visible intermetallics (sample group A), the strength achieved was 86 MPa, a 34% gain over the 65 MPa calculated using the rule-of-mixtures.
3. Heat treatment activates the interdiffusion potential accumulated during roll bonding and governs the intermetallic composition. At 318°C for 30 min (group B), a homogeneous 17–18 μm thick layer forms, delivering a maximum strength of 100 MPa, 55% increase above the value calculated with the rule-of-mixtures.
4. At 328°C for 20 min (group C), Zn penetrates the full Mg inlay, forming a multiphase eutectic and a morphologically complex zone, underscoring the need to refine temperature and strain to achieve controlled interfacial diffusion toward solid-state alloying.

Author Contributions

Yaroslav Frolov: conceptualization (lead), formal analysis (equal), investigation (lead), validation (lead), writing – original draft (equal). **Oleksandr Bobukh:** data curation (equal), investigation (equal), methodology (equal), validation (equal), writing – original draft (supporting). **Christian Klose:** conceptualization (supporting), investigation (supporting), supervision (equal), writing – review & editing (equal). **Florian Nürnberger:** conceptualization (supporting), data curation (equal), investigation (supporting), project administration (lead), writing – original draft (equal), writing – review & editing (equal). **Hans Jürgen Maier:** conceptualization (equal), funding acquisition (lead), project administration (equal), resources (equal), supervision (equal), writing – review & editing (equal).

Acknowledgments

The authors express their sincere gratitude to Dr. Mikhail Rodman for his valuable assistance in conducting the rolling experiments and interpreting the results.

Open Access funding enabled and organized by Projekt DEAL.

Funding

This study was supported by Deutsche Forschungsgemeinschaft (394563137).

Conflicts of Interest

The authors declare no conflicts of interest.

Data Availability Statement

Available upon request.

References

1. A. R. Khan, N. S. Grewal, C. Zhou, K. Yuan, H. Zhang, and Z. Jun, "Recent Advances in Biodegradable Metals for Implant Applications: Exploring In Vivo and In Vitro Responses," *Results in Engineering* 20 (2023): 101526, https://doi.org/10.1016/j.rineng.2023.101526.

2. S. Zhang, X. Zhang, C. Zhao, et al., "Research on an Mg–Zn Alloy as a Degradable Biomaterial," *Acta Biomaterialia* 6, no. 2 (2010): 626–640, https://doi.org/10.1016/j.actbio.2009.06.028.

3. P. Jiang, C. Blawert, and M. L. Zheludkevich, "The Corrosion Performance and Mechanical Properties of Mg-Zn Based Alloys—A Review," *Corrosion and Materials Degradation* 1, no. 1 (2020): 92–158, https://doi.org/10.3390/cmd1010007.

4. Y. Hu, X. Guo, Y. Qiao, X. Wang, and Q. Lin, "Preparation of Medical Mg–Zn Alloys and the Effect of Different Zinc Contents on the Alloy," *Journal of Materials Science: Materials in Medicine* 33, no. 1 (2022): 9, https://doi.org/10.1007/s10856-021-06637-0.

5. D. Cheng, K. Wang, and B. Zhou, "Crystal Structure and Stability of Phases in Mg-Zn Alloys: A Comprehensive First-Principles Study," *Acta Materialia* 242 (2023): 118443, https://doi.org/10.1016/j.actamat.2022.118443.

6. Y. Li, A. Zhang, C. Li, et al., "Recent Advances of High Strength Mg-RE Alloys: Alloy Development, Forming and Application," *Journal of Materials Research and Technology* 26 (2023): 2919–2940, https://doi.org/10.1016/j.jmrt.2023.08.055.

7. B. Zhou, X. Wang, J. Jiang, et al., "Superior Strength-Ductility Synergy of Mg-Nd-Zn-Zr Alloy Rod Achieved by Drawing at Elevated Temperatures," *International Journal of Plasticity* 175 (2024): 103944, https://doi.org/10.1016/j.ijplas.2024.103944.

8. Y. Xie, C. Dong, Z. Liu, Y. Yi, and Y. Zhou, "The Influence of Rolling Reduction on the Mechanical, Corrosion, Osteogenic, and Antibacterial Properties of ZN–MG Alloys," *ACS Omega* 10, no. 33 (2025): 37141–37153, https://doi.org/10.1021/acsomega.5c01732.

9. M. Gieleciak, A. Jarzębska, Ł. Maj, et al., "Influence of Magnesium Addition on Microstructural and Mechanical Stability of Hydrostatically Extruded Biodegradable Zinc Alloys," *Bioactive Materials* 44 (2025): 1–14, https://doi.org/10.1016/j.bioactmat.2024.09.028.

10. J. Lin, Y. Chen, Y. Dai, et al., "Mechanical Properties, Degradation Action, and Biocompatibility of In Situ Nanoparticle-Reinforced MgxZny/Zn Composite Prepared via Roll Bonding," *Acta Biomaterialia* 194 (2025): 514–529, https://doi.org/10.1016/j.actbio.2025.01.048.

11. C. Tang, S. Lyu, R. Zheng, et al., "Realizing Ultra-High Strength and Excellent Ductility in a Low-Alloyed Biomedical Mg-Zn-Ca-MgO Composite," *Journal of Magnesium and Alloys* 12, no. 12 (2024): 5108–5118, https://doi.org/10.1016/j.jma.2024.01.004.

12. W. Fu, P. Dang, S. Guo, et al., "Heterogeneous Fiberous Structured Mg-Zn-Zr Alloy with Superior Strength-Ductility Synergy," *Journal of Materials Science & Technology* 134 (2023): 67–80, https://doi.org/10.1016/j.jmst.2022.06.021.

13. C. Wang, H. Li, F. Liu, et al., "The Investigation of Strength-Ductility Mechanism of Bimodal Size SiCp/Mg–Zn Matrix Composite," *Ceramics International* 50, no. 18 (2024): 32383–32397, https://doi.org/10.1016/j.ceramint.2024.06.046.

14. R. J. H. Navasingh, D. A. Amos, M. K. Gurunathan, and M. P. Nikolova, "Biodegradable MG-ZN-MGO Composites for Locking Compression Fixation Plates for Pediatric Orthopedics: Improved Mechanical Properties and Corrosion Resistance," *Processes* 13, no. 7 (2025): 2077, https://doi.org/10.3390/pr13072077.

15. Q. Sun, D. Zhang, X. Tong, J. Lin, Y. Li, and C. Wen, "Mechanical Properties, Corrosion Behavior, and Cytotoxicity of Biodegradable Zn/Mg Multilayered Composites Prepared by Accumulative Roll

Bonding Process," *Acta Biomaterialia* 173 (2024): 509–525, https://doi.org/10.1016/j.actbio.2023.11.025.

16. W. Wang, X. Zhang, X. Zhang, et al., "High-Performance Mg–Zn Alloy Achieved by the Ultrafine Grain and Nanoparticle Design," *Bioactive Materials* 41 (2024): 371–384, https://doi.org/10.1016/j.bioactmat.2024.07.020.

17. M. Ebrahimi and Q. Wang, "Accumulative Roll-Bonding of Aluminum Alloys and Composites: An Overview of Properties and Performance," *Journal of Materials Research and Technology* 19 (2022): 4381–4403, https://doi.org/10.1016/j.jmrt.2022.06.175.

18. Y. Qi, X. Ma, L. Ma, C. Zhou, Z. Jiang, and J. Zhao, "A Study on the Microstructural Evolution, Interfacial Diffusion and Mechanical Properties of Ultra-Thin Stainless Steel–Copper Composites Fabricated by Roll Bonding," *Metals and Materials International* 30, no. 10 (2024): 2925–2941, https://doi.org/10.1007/s12540-024-01682-0.

19. Y. Xia, Z. Hou, J. Tan, W. Wang, N. Guo, and J. Min, "An Experimental Study on the Frictional Behavior of Ultrathin Metal Sheets at Elevated Temperatures," *Materials* 17, no. 12 (2024): 3009, https://doi.org/10.3390/ma17123009.

20. N. Najafzadeh, M. Z. Quadir, and P. Munroe, "Through Thickness Microstructural and Texture Inhomogeneity Within Al Layers in ARB-Produced Al-Al(Sc) Layered Composite Sheets," *Metallurgical and Materials Transactions A* 46, no. 10 (2015): 4772–4782, https://doi.org/10.1007/s11661-015-3056-4.

21. D. C. C. Magalhães, O. M. Cintho, J. B. Rubert, V. L. Sordi, and A. M. Kliauga, "The Role of Shear Strain during Accumulative Roll-Bonding of Multilayered Composite Sheets: Pattern Formation, Microstructure and Texture Evolution," *Materials Science and Engineering: A* 796 (2020): 140055, https://doi.org/10.1016/j.msea.2020.140055.

22. X. Mei, Q. Mei, J. Li, et al., "Solid-State Alloying of Al-Mg Alloys by Accumulative Roll-Bonding: Microstructure and Properties," *Journal of Materials Science & Technology* 125 (2022): 238–251, https://doi.org/10.1016/j.jmst.2022.02.029.

23. Z. Han, B. Liu, Q. Fang, P. K. Liaw, and J. Li, "A Dislocation Theory-Based Model for Brittle-to-Ductile Transition in Multi-Principal Element Alloys," *International Journal of Plasticity* 180 (2024): 104059, https://doi.org/10.1016/j.ijplas.2024.104059.

24. K. Tang, Y. Xiang, J. Tian, et al., "Machine Learning-Based Morphological and Mechanical Prediction of Kirigami-Inspired Active Composites," *International Journal of Mechanical Sciences* 266 (2024): 108956, https://doi.org/10.1016/j.ijmecsci.2023.108956.

25. Y. Frolov, O. Bobukh, A. Samsonenko, and F. Nürnberger, "Patterning of Surfaces for Subsequent Roll Bonding in a Low-Oxygen Environment Using Deformable Mesh Inlays," *Journal of Manufacturing and Materials Processing* 7, no. 5 (2023): 158, https://doi.org/10.3390/jmmp7050158.

26. G. Chaudhary, L. Niu, Q. Han, M. Lewicka, and L. Mahadevan, "Geometric Mechanics of Ordered and Disordered Kirigami," *Proceedings of the Royal Society A: Mathematical, Physical and Engineering Sciences* 479, no. 2274 (2023): 20220822, https://doi.org/10.1098/rspa.2022.0822.

27. Y. Frolov, D. Konovodov, O. Bobukh, and V. Boiarkin, "Transformation of the Kirigami-Type Deformable Inlay during Roll Bonding," *Naukovyi Visnyk Natsionalnoho Hirnychoho Universytetu* no. 1 (2025): 34–39, https://doi.org/10.33271/nvngu/2025-1/034.

28. Y. Frolov, F. Nuernberger, D. Konovodov, O. Bobukh, and V. Boiarkin, "Influence of Deformation Parameters on Mechanical Behaviour of Aluminium-Magnesium Roll-Bonded Composites with Kirigami-Structured Inlays," *Naukovyi Visnyk Natsionalnoho Hirnychoho Universytetu* no. 5 (2025): 69–77, https://doi.org/10.33271/nvngu/2025-5/069.

29. Y. Frolov, Y. Haranich, O. Bobukh, O. Remez, D. Voswinkel, and O. Grydin, "Deformation of Expanded Steel Mesh Inlay inside Aluminum Matrix during the Roll Bonding," *Journal of Manufacturing Processes* 58 (2020): 857–867, https://doi.org/10.1016/j.jmapro.2020.08.049.

30. Y. Frolov, M. Nosko, A. Samsonenko, O. Bobukh, and O. Remez, "Roll Bonding of Al-Based Composite Reinforced with C10 Steel Expanded Mesh Inlay," *Metals* 11, no. 7 (2021): 1044, https://doi.org/10.3390/met11071044.

31. G. Simons, C. Weippert, J. Dual, and J. Villain, "Size Effects in Tensile Testing of Thin Cold Rolled and Annealed Cu Foils," *Materials Science and Engineering: A* 416, no. 1-2 (2006): 290–299, https://doi.org/10.1016/j.msea.2005.10.060.

32. A. Mucsi, "Experimental Investigation of Stress Distribution in a Tensile Test Specimen, Using a Novel Gripping System for Tensile Testing," in *Topics in Intelligent Engineering and Informatics*, (Springer, 2016), 153–161, https://doi.org/10.1007/978-3-319-28091-2_13.

33. H. Liu, H. Huang, Y. Zhang, et al., "Evolution of Mg–Zn Second Phases during ECAP at Different Processing Temperatures and Its Impact on Mechanical Properties of Zn-1.6Mg (wt.%) Alloys," *Journal of Alloys and Compounds* 811 (2019): 151987, https://doi.org/10.1016/j.jallcom.2019.151987.

34. X. Li, Y. Wang, H. M. Soltani, and M. Tayebi, "Roll Bonding Characteristics of the Mg/Zn/Cu/Al Multilayered Composite Produced by the ARB Process," *Materials Letters* 369 (2024): 136720, https://doi.org/10.1016/j.matlet.2024.136720.

35. A. Chapuis and Q. Liu, "Modeling Strain Rate Sensitivity and High Temperature Deformation of Mg-3Al-1Zn Alloy," *Journal of Magnesium and Alloys* 7, no. 3 (2019): 433–443, https://doi.org/10.1016/j.jma.2019.04.004.

36. H. Yu, D. Yeon, A. Van Der Ven, and K. Thornton, "Substitutional Diffusion and Kirkendall Effect in Binary Crystalline Solids Containing Discrete Vacancy Sources and Sinks," *Acta Materialia* 55, no. 20 (2007): 6690–6704, https://doi.org/10.1016/j.actamat.2007.08.031.

37. C. Chen, W. Zheng, Z. Wang, R. Li, and B. Wang, "Effect of Additional Solutes on the Vacancy-Mediated Diffusion of Mg in Biodegradable Zn-Based Alloys: A First-Principles Study," *Journal of Materials Research and Technology* 33 (2024): 9221–9231, https://doi.org/10.1016/j.jmrt.2024.11.229.